ACOUSTIC WAVE PROPAGATION IN STANDING TREES—PART I. NUMERICAL SIMULATION

Fenglu Liu

PhD candidate
School of Technology
Beijing Forestry University
Beijing, China
E-mail: liufenglu39@126.com

*Xiping Wang**†*

Research Forest Products Technologist, PhD
USDA Forest Service
Forest Products Laboratory
Madison, WI
E-mail: xiping.wang@usda.gov

*Houjiang Zhang***

Professor
E-mail: hjzhang6@bjfu.edu.cn

Fang Jiang

Associate Professor
E-mail: jf0602@bjfu.edu.cn

Wenhua Yu

Professor
School of Technology
Beijing Forestry University
Beijing, China
E-mail: yuwenhua56@sina.com

Shanqing Liang

Associate Professor
E-mail: liangsq@caf.ac.cn

Feng Fu

Professor, Director
Research Institute of Wood Industry
Chinese Academy of Forestry
Beijing, China
E-mail: feng@caf.ac.cn

* Corresponding authors
† SWST member

Wood and Fiber Science, 52(1), 2020, pp. 53-72
https://doi.org/10.22382/wfs-2020-006

Robert J. Ross

Acting Assistant Director
USDA Forest Service
Forest Products Laboratory
Madison, WI
E-mail: robert.j.ross@usda.gov

(Received July 2019)

Abstract. The use of acoustic waves for assessing wood properties in standing trees has been investigated extensively in recent years. Most studies were experimental in nature and limited to direct measurement of wave velocities in trees using a time-of-flight (TOF) method. How acoustic waves propagate in a tree trunk and how tree diameter, species, stand age, and juvenile wood affect wave propagation behavior in standing trees are not well understood. In this study, we examined propagation patterns of acoustic waves in a virtual tree trunk through numerical simulation using COMSOL Multiphysics® software (COMSOL, Inc., Burlington, MA). The simulation was based on the elastic theory of a solid medium with the assumption of an orthotropic material for a standing tree. Extensive acoustic measurements were conducted on green larch log samples to validate the simulation results. Our results showed that the wave front maps of the tree model from numerical simulations were consistent with those obtained through TOF measurements on the log samples, indicating that the simulation results were accurate and reliable. Wave propagation patterns of the tree model revealed that the side surface–generated acoustic wave expanded as a dilatational wave within a 0- to 1.2-m transit distance; as the wave moved up along the tree model, the shape of the wave front gradually flattened and the wave eventually transformed into a quasi-plane wave from a 2.4-m transit distance.

Keywords: Acoustic waves, boundary condition, COMSOL Multiphysics software, impulse load, orthotropic material, wave front, trees.

INTRODUCTION

Acoustic wave technology has been widely recognized as an effective nondestructive testing tool for assessing raw wood materials in forest operations and wood-manufacturing processes (Wang et al 2007b). The technology was initially developed for rapidly and nondestructively evaluating and grading structural timber and wood-based composite materials (such as veneer, laminated veneer lumbers, and glued laminated timber) (Sharp 1985; Ross and Pellerin 1988; Arima et al 1990; Aratake et al 1992; Aratake and Arima 1994; Brashaw et al 1996; Halabe et al 1997). Because of the strong relationships between the acoustically determined dynamic MOE of logs and the static MOE of the end products (eg structural lumber and laminated veneer lumber), acoustic wave technology is increasingly being used to evaluate the incoming logs in sawmills and sort logs into appropriate classes (Addis et al 1997; Ross et al 1997; Addis et al 2000; Matheson et al 2002; Carter and Lausberg 2003; Wang et al 2004a; Carter et al 2005, 2006; Amishev and Murphy 2008). In addition, many studies conducted on standing trees showed good correlations between acoustic wave velocity measured in trees and those measured in logs. This has opened the way for acoustic-based sensing technology to be applied in the forest for evaluating and sorting standing trees (Nanami et al 1992a, 1992b, 1993; Lindström et al 2002; Chauhan and Walker 2006; Grabianowski et al 2006; Wang et al 2007a; Matheson et al 2008; Raymond et al 2008; Mora et al 2009).

Acoustic wave velocity has been used to predict MOE, generally referred to as the dynamic MOE, of standing trees by measuring the time of flight (TOF) of acoustic waves between two measuring points (typically centered around tree's breast height and spanning about 1.2 m). This tree acoustic measurement, typically called the TOF method, involves inserting two sensor probes (transmitter and receiver probes) into the tree trunk and introducing acoustic energy into the tree through a hammer impact. Research on using the TOF method to assess wood properties of trees has been mostly experimental and limited to direct measurement of acoustic velocity in standing trees.

Subsequent wood property prediction and evaluation are solely based on the measured TOF velocity of the trees (Wang 1999, 2013; Paradis et al 2013; Amateis 2015; Gil-Moreno and Dan 2015; Trejo 2015; Legg and Bradley 2016; Madhoushi and Daneshvar 2016).

Although TOF acoustic measurement has been proven to be a rapid and robust method for assessing wood mechanical properties in standing trees, how acoustic waves propagate in a tree stem and how the tree diameter, species, stand age, and juvenile wood affect wave propagation in trees are not well understood (Wang 2013; Legg and Bradley 2016). Results of numerous field studies performed on trees of different species and stand ages revealed that acoustic velocities measured on standing trees using the TOF method were 7-36% higher than the corresponding log velocity measured using a resonance acoustic method, ie the ratio of the tree TOF velocity to the log resonance velocity ranged from 1.07 to 1.36 (Wang 2013). Using the TOF velocity to predict wood stiffness would result in overestimation (Wang 1999; Andrews 2003; Wang et al 2003; Chauhan and Walker 2006; Grabianowski et al 2006; Lasserre et al 2007; Wang et al 2007b; Mora et al 2009). Several different explanations have been offered on why tree velocities deviate from log velocities. One explanation discussed in many articles is that the single-pass transit-time velocities measured in tree stems using the TOF method are sensitive to the high localized stiffness of the outer wood lying in the "flight path" between the two probes, whereas the resonance-based acoustic methods used to test logs assess area-weighted cross-sectional average stiffness (Chauhan and Walker 2006; Grabianowski et al 2006; Mora et al 2009). Another interpretation for this velocity difference given in several articles is linked to different wave propagation mechanisms of these two different acoustic approaches (Wang et al 2007a; Zhang et al 2011; Wang 2013). They suggested that acoustic wave propagation behavior in standing trees is likely dominated by dilatational waves rather than one-dimensional plane waves in logs. Consequently, in the case of standing trees, the dynamic MOE of wood should be determined using the dilatational wave equation instead of the rod wave equation, which is used in many articles.

In addition to different wave propagation mechanisms associated with the TOF and resonant acoustic methods, Wang (2013) argued that the tree velocity deviation may also be related to the tree diameter, stand age of trees, and proportion of juvenile wood in tree cross sections. Some correlative relationships between the tree diameter and acoustic velocity measured in trees (or stiffness calculated from it) have been reported for different softwood species (Wang et al 2003; Lasserre et al 2004, 2005; Carter et al 2005; Chauhan and Walker 2006). Based on field experimental data, Wang et al (2003, 2007a) proposed empirical and analytical models for adjusting tree velocity measured using the TOF method to the corresponding log velocity measured using the acoustic resonance method. Both models were found effective in eliminating deviation between tree and log velocities and reducing variability in velocity prediction. However, these models are experimental in nature and, thus, valid only to the species and stands investigated in the study.

In this study, we attempted to simulate acoustic wave propagation in a virtual tree trunk through numerical simulation using COMSOL Multiphysics software (COMSOL, Inc.) and examine the propagation patterns of longitudinal acoustic waves in standing trees. The simulation was based on the elastic theory of the solid medium with the assumption of the orthotropic material for standing trees. The specific objectives were to 1) examine the validity of the tree model and use of COMSOL Multiphysics software for conducting accurate numerical simulations; 2) determine the wave fronts of acoustic waves as they are initiated through a mechanical impact on the side of a standing tree; and 3) investigate the effects of the tree diameter, transit distance, and proportion of juvenile wood on wave fronts and wave velocities.

This report is part 1 of a series of articles on the investigation of acoustic wave propagation in standing trees. The objective of this report was to examine the propagation patterns of acoustic waves in trees and logs based on the fundamental

wave theory of solid medium with the assumption of the orthotropic material for a tree stem using the COMSOL Multiphysics software. Three-dimensional wave propagation patterns in virtual tree and log models were obtained and compared. The effect of the tree diameter, propagation distance, and juvenile wood on wave propagation will be reported in part 2.

ORTHOTROPIC MECHANICAL PROPERTIES OF WOOD

Wood is a complex biological material with unique cell wall structures and variable physical and mechanical properties. In general, wood can be described as an orthotropic material, ie it has unique and independent mechanical properties in three mutually perpendicular axes: longitudinal, radial, and tangential directions. The longitudinal axis L is parallel to the fiber (grain); the radial axis R is normal to the growth rings (perpendicular to the grain in the radial direction); and the tangential axis T is perpendicular to the grain but tangential to the growth rings. For a tree stem, a cylindrical coordinate system with orthotropic axes in the longitudinal, radial, and tangential directions can be used to characterize the mechanical behavior of wood in trees.

In linear elasticity, the relation between stress and strain depends on the type of material under consideration. This relation is known as Hooke's law. For orthotropic wood material, the stress–strain relationship can be expressed as follows:

$$\boldsymbol{\sigma} = \mathbf{C} : \boldsymbol{\varepsilon}, \tag{1}$$

where $\boldsymbol{\sigma}$ is the stress tensor, $\mathbf{C}$ is the elastic stiffness tensor, and $\boldsymbol{\varepsilon}$ is the strain tensor. When these three tensors are expanded in the form of base vectors, Eq (1) becomes

$$\sigma_{ij} = C_{ijkl}\varepsilon_{kl}, \quad (i,j,k,l = 1,2,3), \tag{2}$$

where i, j, k, and l are coordinate indices, each can independently attain the values of 1, 2, or 3. The convention for σ_{ij} is that subscript i, which indicates the direction of stress force, and j defines which face the stress is applied to.

The law in the form given in Eq (2) contains redundancies because of the symmetry characteristics of the stress and strain matrices. When symmetry is considered, $\sigma_{ij} = \sigma_{ji}$; then, Hooke's law takes a much simpler form. For orthotropic materials, the elastic stiffness tensor $\mathbf{C}$ is a fourth-order symmetric tensor, so the components of the elastic stiffness tensor can be represented by a sixth-order matrix:

$$\left[C_{ijkl}\right] = \begin{bmatrix} C_{1111} & C_{1122} & C_{1133} & 0 & 0 & 0 \\ C_{1122} & C_{2222} & C_{2233} & 0 & 0 & 0 \\ C_{1133} & C_{2233} & C_{3333} & 0 & 0 & 0 \\ 0 & 0 & 0 & C_{1212} & 0 & 0 \\ 0 & 0 & 0 & 0 & C_{2323} & 0 \\ 0 & 0 & 0 & 0 & 0 & C_{1313} \end{bmatrix}. \tag{3}$$

The components of the elastic stiffness tensor can be represented using a simplified index system and replaced with an elastic stiffness matrix D:

$$[D] = \begin{bmatrix} D_{11} & D_{12} & D_{13} & 0 & 0 & 0 \\ D_{12} & D_{22} & D_{23} & 0 & 0 & 0 \\ D_{13} & D_{23} & D_{33} & 0 & 0 & 0 \\ 0 & 0 & 0 & D_{44} & 0 & 0 \\ 0 & 0 & 0 & 0 & D_{55} & 0 \\ 0 & 0 & 0 & 0 & 0 & D_{66} \end{bmatrix} = \begin{bmatrix} C_{1111} & C_{1122} & C_{1133} & 0 & 0 & 0 \\ C_{1122} & C_{2222} & C_{2233} & 0 & 0 & 0 \\ C_{1133} & C_{2233} & C_{3333} & 0 & 0 & 0 \\ 0 & 0 & 0 & C_{1212} & 0 & 0 \\ 0 & 0 & 0 & 0 & C_{2323} & 0 \\ 0 & 0 & 0 & 0 & 0 & C_{1313} \end{bmatrix}, \tag{4}$$

where subscripts 1, 2, and 3 refer to the longitudinal, tangential, and radial stiffness and subscripts 4, 5, and 6 are a shorthand notation that refers to the shearing stiffness.

The stiffness matrix D is also normally expressed in terms of its inverse matrix S, which is referred to as the compliance matrix:

$$[S] = \begin{bmatrix} S_{11} & S_{12} & S_{13} & 0 & 0 & 0 \\ S_{12} & S_{22} & S_{23} & 0 & 0 & 0 \\ S_{13} & S_{23} & S_{33} & 0 & 0 & 0 \\ 0 & 0 & 0 & S_{44} & 0 & 0 \\ 0 & 0 & 0 & 0 & S_{55} & 0 \\ 0 & 0 & 0 & 0 & 0 & S_{66} \end{bmatrix}. \quad (5)$$

For an orthotropic material such as wood, an alternative notation (L, R, and T) is commonly used in the 6 × 6 compliance matrix (substitute L for 1, R for 2, and T for 3):

$$[S] = \begin{bmatrix} \frac{1}{E_1} & -\frac{\upsilon_{12}}{E_2} & -\frac{\upsilon_{13}}{E_3} & 0 & 0 & 0 \\ -\frac{\upsilon_{21}}{E_1} & \frac{1}{E_2} & -\frac{\upsilon_{23}}{E_3} & 0 & 0 & 0 \\ -\frac{\upsilon_{31}}{E_1} & -\frac{\upsilon_{32}}{E_2} & \frac{1}{E_3} & 0 & 0 & 0 \\ 0 & 0 & 0 & \frac{1}{G_{23}} & 0 & 0 \\ 0 & 0 & 0 & 0 & \frac{1}{G_{13}} & 0 \\ 0 & 0 & 0 & 0 & 0 & \frac{1}{G_{12}} \end{bmatrix}, \quad (6)$$

where E_L, E_R, and E_T are the elastic modulus of wood in the longitudinal, radial, and tangential directions; G_{LR}, G_{LT}, and G_{RT} are the shear modulus; and υ_{LR}, υ_{RL}, υ_{LT}, υ_{TL}, υ_{RT}, and υ_{TR} are the Poisson's ratios. Generally, the stiffness and compliance matrices are both hypothesized to be symmetric, for instance, $D_{ij} = D_{ji}$ and $S_{ij} = S_{ji}$.

Among the 12 elastic parameters that describe the mechanical behavior of wood materials, the longitudinal stiffness (E_L) is the most important wood property that concerns wood manufacturers and engineers in producing various wood products, particularly structural lumber and engineered wood products (such as glued laminated timber, laminated veneer lumber, and cross-laminated timber). Consequently, wood stiffness has been the most researched wood quality index in recent decades. Various nondestructive methods have been developed to determine the longitudinal stiffness of wood in the long slender form. One example is the acoustic resonance technique currently being implemented in mills and log yards for grading structural timber and sorting incoming logs based on stiffness measures (Addis et al 1997, 2000; Wang et al 2007b).

The other elastic stiffness values of wood are usually determined through mechanical tests of small clear specimens in the laboratory, and their mean values for individual species are available in the literature (Bodig and Jayne 1982; Forest Products Laboratory 2010). Poisson's ratios of wood reported in most of the literature are for dry wood, and they appear to change with species and material sources. Statistical analysis by Bodig and Goodman (1973) indicated that Poisson's ratios do not seem to vary with density or other anatomical characteristics of wood in any recognized fashion. Therefore, an average value of 0.37 (υ_{LR}) has been suggested for both softwoods and hardwoods (Bodig and Goodman 1973). However, Poisson's ratios of green wood are not explicitly known (Wang 2013).

FUNDAMENTAL WAVE THEORY

A basic understanding of the relationship between wood stiffness and longitudinal wave velocity can be acquired from the fundamental wave theory. In a long, slender, and isotropic rod, strain and inertia in the radial direction can be neglected and the compressional waves propagate in a plane wave (wave front). In this ideal case, the wave velocity is independent of Poisson's ratio and is given by the following equation

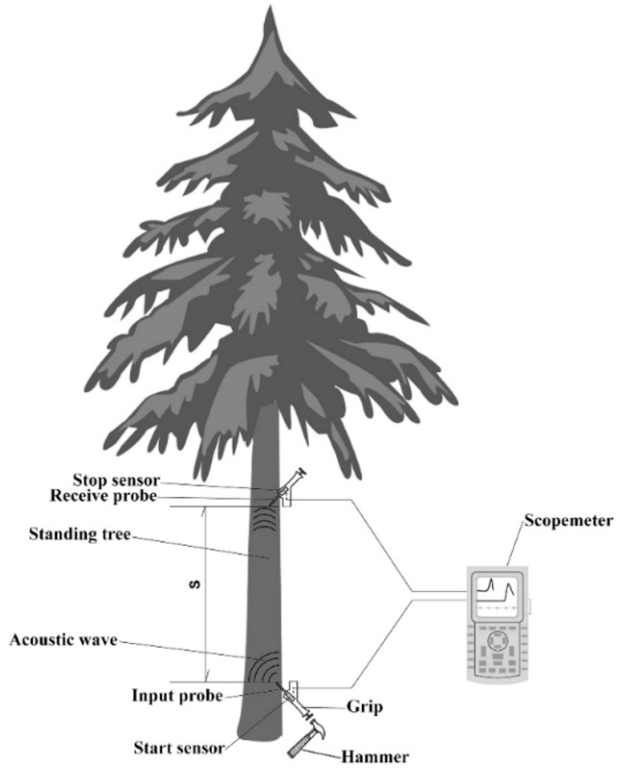

Figure 1. Time-of-flight acoustic measurement on a standing tree.

(hereafter referred to as a one-dimensional wave equation):

$$C_0 = \sqrt{\frac{E_L}{\rho}}, \tag{7}$$

where C_0 is longitudinal wave velocity in the rod, E_L is longitudinal MOE, and ρ is mass density of the material. Eq (7) is often used in studies to predict the MOE of structural timber, logs, and utility poles by measuring the acoustic wave velocity and wood density (Ross et al 1997; Carter and Lausberg 2003; Wang et al 2007b).

Table 1. Average elastic constant values and density of the model.

MOE (MPa)[a]		Modulus of rigidity (MPa)[b]		Poisson's ratio[c]		Density (kg/m^3)
E_L	7629	G_{RT}	450	υ_{LR}	0.22	625
E_R	773	G_{LR}	428	υ_{RL}	0.05	
E_T	362	G_{LT}	393	υ_{LT}	0.30	
				υ_{TL}	0.04	
				υ_{TR}	0.60	
				υ_{RT}	0.77	

[a] E_L, longitudinal MOE; E_R, radial MOE; E_T, tangential MOE.
[b] G_{RT}, shear modulus in *R-T* plane; G_{LR}, shear modulus in *L-R* plane; G_{LT}, shear modulus in *L-T* plane.
[c] υ_{LR}, υ_{RL}, υ_{LT}, υ_{TL}, υ_{TR}, and υ_{RT} are Poisson's ratio.

In an infinite or unbounded isotropic elastic medium, a triaxial state of stress is present. The wave front of the longitudinal wave propagating through such a medium is no longer a plane. The wave propagation is governed by the following three-dimensional longitudinal wave equation (Meyers 1994):

$$C_L = k\sqrt{\frac{E_L}{\rho}}, \tag{8}$$

where C_L is the dilatational wave velocity, E_L is the longitudinal MOE of the medium, and k is a term related to Poisson's ratios of wood,

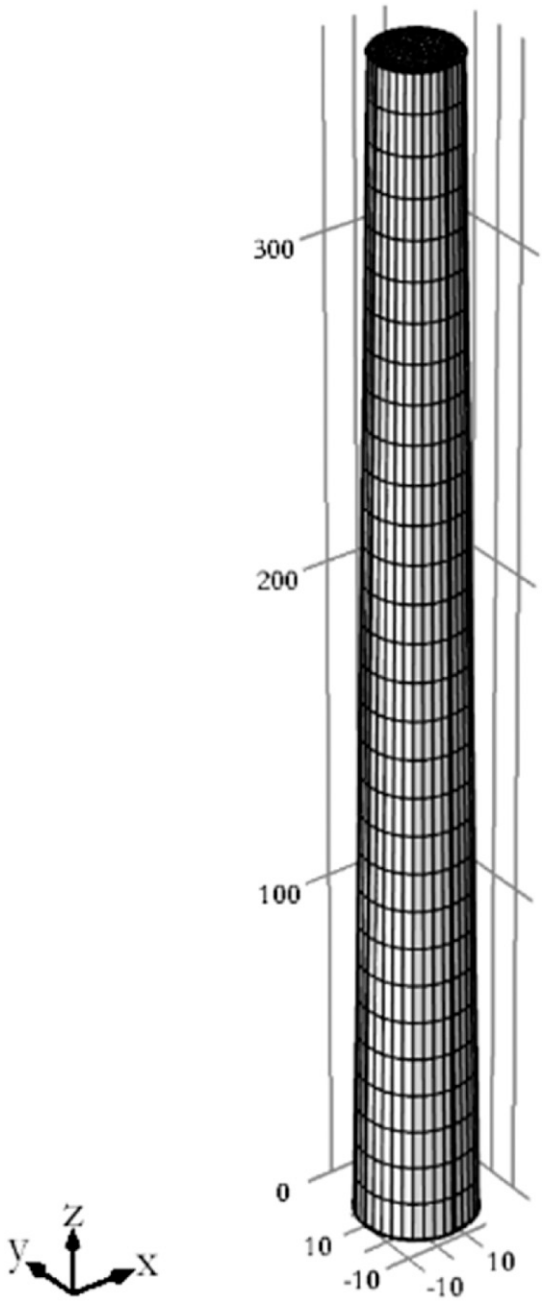

Figure 2. Three-dimensional geometry model of a standing tree with divided grids.

$$k = \sqrt{\frac{1-\nu}{(1+\nu)(1-2\nu)}}. \tag{9}$$

Therefore, the wave velocity is dependent on the elastic modulus, Poisson's ratio, and density of the material.

For an orthotropic medium, the term k is given by

$$k = \sqrt{\frac{1-\nu_{RT}\nu_{TR}}{1-\nu_{RT}\nu_{TR}-\alpha}}, \tag{10}$$

where $\alpha = 2\nu_{RL}\nu_{TR}\nu_{LT} + \nu_{TL}\nu_{LT} + \nu_{RL}\nu_{LR}$ and ν_{RL}, ν_{LR}, ν_{TL}, ν_{LT}, ν_{TR}, and ν_{RT} are the Poisson's ratios in *RL*, *LR*, *TL*, *LT*, *TR*, and *RT* planes of the orthotropic medium.

Consequently, the theoretical dilatational wave velocity in an infinite or unbounded orthotropic medium can be obtained from the following equation:

$$C_L = k\sqrt{\frac{E_L}{\rho}} = \sqrt{\frac{1-\nu_{RT}\nu_{TR}}{1-\nu_{RT}\nu_{TR}-\alpha}\,\frac{E_L}{\rho}}. \tag{11}$$

NUMERICAL SIMULATION OF WAVE PROPAGATION IN TREES

The initiation of acoustic waves in a standing tree is through a mechanical impact on a spiked probe inserted into the trunk. This is very different from the acoustic resonance testing on a log, in which acoustic waves are introduced into the log by a direct hammer impact at the end. A typical approach for in situ TOF acoustic measurement in trees involves inserting two sensor probes (transmit probe and receiver probe) into the sapwood at about 45° to the tree surface, angled toward each other, and introducing an impulse burst into the tree trunk through a hammer impact (Fig 1). The test span is usually limited to 1 to 1.22 m, so that the TOF measurements can be readily carried out by an operator. Field acoustic measurements mainly concern the tree trunk in the test span, but our simulations run a greater distance (up to 3.2 m) to illustrate the progressive changes of the acoustic waves along the tree trunk.

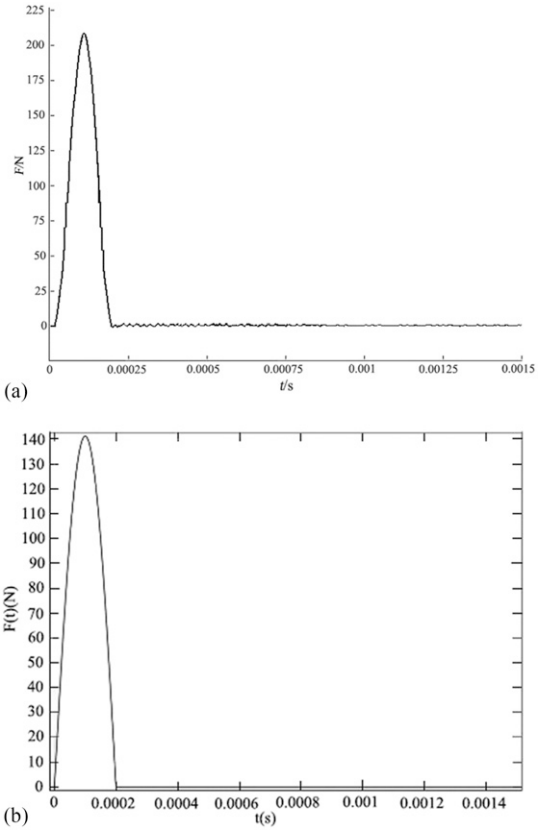

Figure 3. Impact pulse used to generate acoustic waves in standing trees. (a) Signal of an actual impact pulse; (b) half-sine function of a simulated impact pulse.

Modeling for Trees

Geometry model and material properties. The plantation trees considered in this study were 40-yr-old larch (*Larix principis-rupprechtii* Mayr) with a diameter at breast height from 14 to 37.5 cm and a taper from 1 to 3 cm per meter (based on measurements on 50 sampled trees). The tree trunks to be modeled were considered as orthotropic cylindrical medium with elastic parameters and wood density provided in Table 1. The axial (L), radial (R), and tangential (T) directions of the model were defined as three principal axes x, y, and z in a Cartesian coordinate system. The model was further simplified by the following assumptions: 1) homogenous medium from pith to bark, 2) no growth rings, and 3) no natural defects.

Twelve elastic constants of green larch were determined through laboratory experiments in a previous study (Liu et al 2015). The wood specimens used to determine the elastic constants were cut from three larch logs harvested in a 40-yr-old larch plantation stand located in Chengde, China. The average values of 12 elastic constants and the gross density of green larch are shown in Table 1.

Considering the symmetry of a trunk's form and taking both the efficiency of calculation and the tree's taper into consideration, we set the geometry model of larch trees as a tapered cylinder of 3.6 m length, with a large-end diameter of 35 cm and a small-end diameter of 25 cm. Figure 2 shows the three-dimensional geometry model of plantation trees constructed with COMSOL software.

Impulse load. Acoustic waves used in tree measurements are typically produced through a mechanical impact on the transmit probe (start sensor), and this impact-induced stress wave has a very short duration. Figure 3(a) shows an example of an actual impact pulse generated in the laboratory by using a hammer to create an impact on a Fakopp spike sensor. To mimic the actual impact pulse, we used the following half-sine pulse function to express this impact force:

$$F(t) = \begin{cases} A\ \sin(2\pi ft), & t < (1/2f) \\ 0, & t \geq (1/2f) \end{cases}, \qquad (12)$$

where A is the amplitude of the impact pulse and f is frequency of the sine wave.

The amplitude of the actual impact pulse was calibrated to an impact force of 200 N. The width of the impact pulse was measured as 0.2 ms, which corresponds to a frequency of 2.5 kHz in a sine wave.

The transmit sensor probe is inserted into the tree trunk at a 45° angle with respect to the trunk's longitudinal axis. Thus, the impact force $F(t)$ acting on the start sensor can be decomposed into two orthogonal components, $F_y(t)$ and $F_z(t)$, and

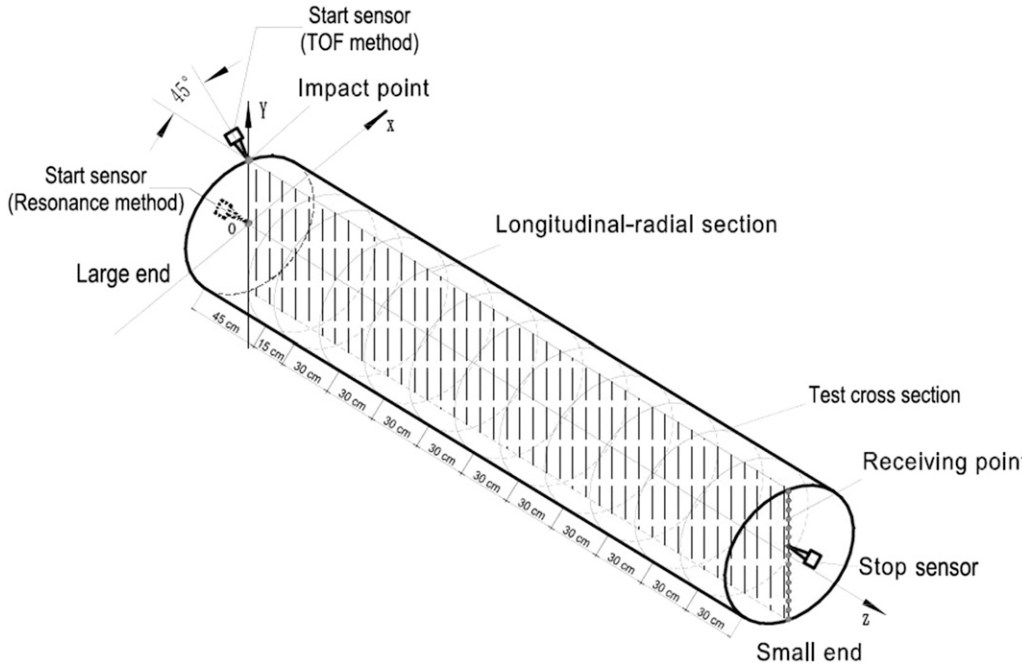

Figure 4. Schematic diagram of conducting field time-of-flight acoustic measurements on log samples that mimic both tree and log acoustic measurements.

the amplitude of each component is 141.4 N. Figure 3(b) shows the input function of the orthogonal component of the impact force.

Initial and boundary conditions. The particles of a tree model are in a static state before an impulse loading. The initial displacement and initial velocity of each particle in the model were, therefore, set as zero. Two boundary condition cases were examined for the wave propagation simulation. In the first case, we applied the low-reflection boundary condition to both the side surface and the two ends of the tree model. The low-reflecting boundary condition is also called nonreflecting or silent boundary condition and can be described as follows:

$$\left.\frac{\partial u}{\partial l}\right|_{(x^2+y^2=d^2,0\le z\le 360)}=0, \qquad (13)$$

where u is the displacement of particle, l is the unit normal vector at the boundary, and d is the radius of the model.

The low-reflecting boundary condition allows waves to pass through the model domain without reflection. That is, when the waves reach the boundary of the tree model, only compression waves exist, with no reflected wave or a very small amount of reflected wave (Cohen and Jennings 1983).

In the second case, two ends of the tree model were kept with the low-reflection condition, but the side surface of the tree model was set to have a free boundary condition in which the compression waves and reflected waves coexist with wave attenuation when acoustic wave propagates to the side boundary of the tree model (Lalanne and Touratier 2000). The free boundary condition can be described as follows:

$$\sigma\cdot n=-\rho\cdot C_{\mathrm{p}}\left(\frac{\partial u}{\partial t}\cdot n\right)\cdot n-\rho\cdot C_{\mathrm{s}}\left(\frac{\partial u}{\partial t}\cdot t\right)\cdot t, \qquad (14)$$

where σ is the stress, n and t are unit normal and tangential vectors at the boundary, and C_{p} and C_{s}

Figure 5. A special pendulum device mounted onto the upper side of the log to generate constant impacts on the start sensor.

are speeds of the pressure and shear waves in the material, respectively.

The combination of free and low-reflection boundary conditions in the second case were believed to be more realistic than the low-reflection boundary alone, considering the fact that no constraints or loads are actually acting on the circumferential surfaces except the source point where the impulse load is initiated.

When the commonly used free meshing (ie the tetrahedral elements method) was used in the three-dimensional tree model, the number of meshes generated was too large because of the relatively large model dimension, and it resulted in a surge in computational complexity for the numerical simulation. Therefore, we decided to use a sweep method to get a reasonable number of grids. The largest and smallest elements in the ends of the tree model were 1.4 cm and 0.004 cm, respectively. After the meshing of the end surface was completed, the sweep method was used to extend the mesh to the whole tree model. The total number of meshes obtained for the model was up to 44,000. The divided grids of the tree model are shown in Fig 2.

Modeling for Logs

Acoustic velocities in logs are typically measured using a resonance-based approach. In log acoustic resonance measurement, an acoustic sensor is mounted on one end of a log. An acoustic wave is initiated by a mechanical impact on the end, and the acoustic waveforms are subsequently recorded by an electronic unit. In contrast to the TOF approach, the resonance method stimulates many, possibly hundreds, of acoustic pulse reverberations in a log, resulting in a very accurate and repeatable velocity measurement. Because of this accuracy, the acoustic velocity of logs obtained by the resonance-based measurement has served as a standard to validate the TOF measurement in standing trees (Wang 1999; Wang et al 2001; Andrews 2003; Carter et al 2005).

To better understand the differences between TOF in trees and resonance measurement in logs, we also conducted numerical simulation of longitudinal acoustic waves in a log model. The geometry, initial conditions, boundary conditions, and meshing for the log model are the same as those for the tree model, except it is turned 90° from the tree model, with the impact source point located at the center of the log end. The mechanical impact force is expressed using the same half-sine pulse function (Eq [12]) as in the tree modeling. Because the direction of impact force is perpendicular to the end gain, which is in the longitudinal direction, the amplitude of the pulse was set to 200 N.

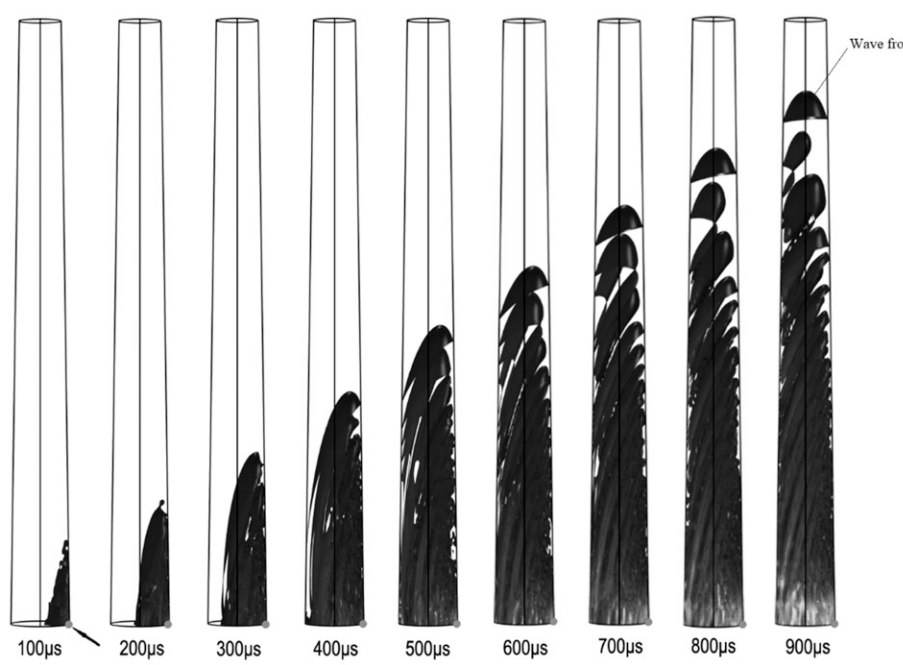

(a) Low-reflection boundaries

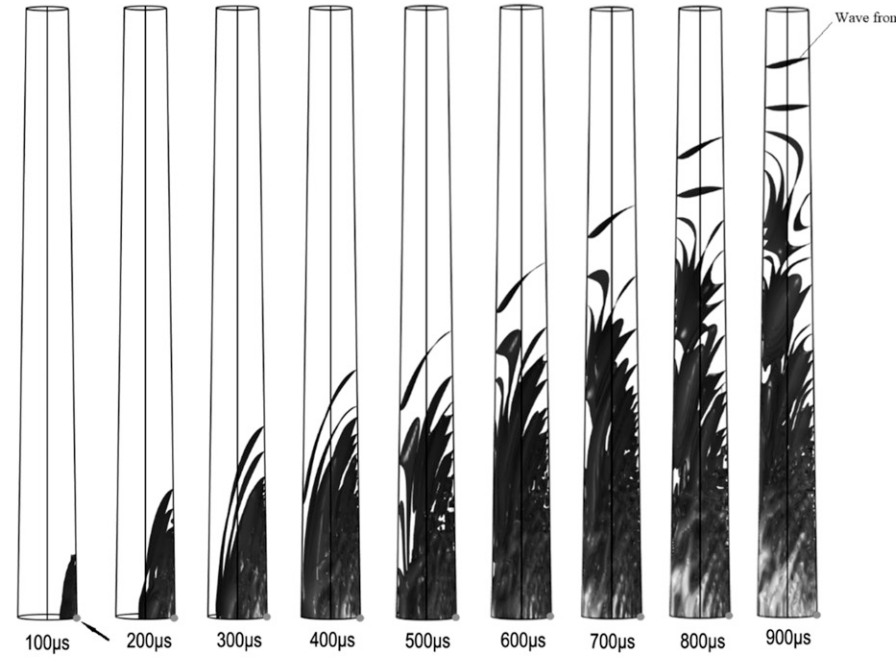

(b) Free and low-reflection boundaries

Figure 6. Contour surface maps of total displacements in the tree model at various time points. (a) Low-reflection boundary (side and ends); (b) free (side) and low-reflection (ends) boundaries.

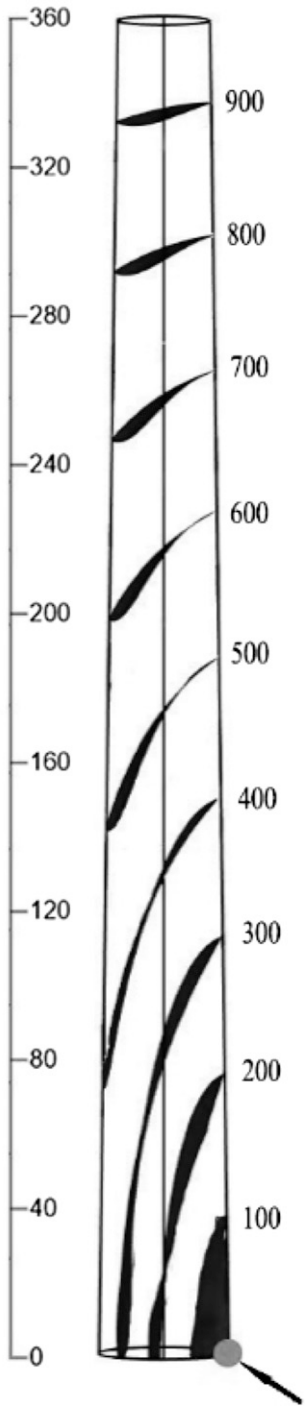

Figure 7. Wave front progression maps of the tree model (unit: μs; the dot in the lower right corner indicates the wave initiation point).

EXPERIMENTAL VALIDATION

To validate the numerical simulation results of wave propagation in trees and logs, we conducted extensive acoustic measurements on green larch log samples to physically map the progression of the wave fronts in a time sequence. Three larch trees of different diameters were selected and harvested at a 40-yr-old plantation stand in the Maojingba national plantation forest, Chengde, Hebei Province, China (118°06′05″E, 41°28′46″N, 750 m elevation). A 3.6-m-long butt log was obtained from each felled tree. The diameters of these three logs were 38, 32, and 28 cm in the large end and 31, 27, and 24 cm, respectively, in the small end.

Figure 4 shows the schematic diagram for conducting TOF acoustic wave measurements that mimic both tree (impact source on the side surface of tree trunk) and log (impact source on the end grain of log end) acoustic measurements. TOF measurements were performed when the log samples were laid flat on the ground in the forest. The measurement system included a battery-operated stress wave timer (Fakopp Microsecond Meter, Fakopp Enterprise, Ágfalva, Hungary), two spike-type transducers, a small hammer, and a pendulum device.

To mimic tree measurement, the start sensor probe was mounted on the upper side of the log surface, close to the large end, by inserting the spike 1 cm deep, at a 45° angle with respect to the upper surface; the stop sensor probe was mounted at the cross section of the small end by inserting the spike 1-cm deep into the end grain. The start sensor remained in the same position during the measurement process, whereas the position of the stop sensor was continuously changed along the vertical middle lines on the small end (Fig 4). A constant impact on the start sensor probe was generated by a special pendulum device mounted onto the log (Fig 5). The stop sensor received acoustic wave signals, and the TOF data were displayed and recorded. A series of TOF measurements were conducted by moving the stop sensor probe to different locations at the middle vertical line on the end cross section, with 25-mm increments. Once the TOF measurements were completed at one end cross section, a 30-cm long section was cut off from the small end, and the same

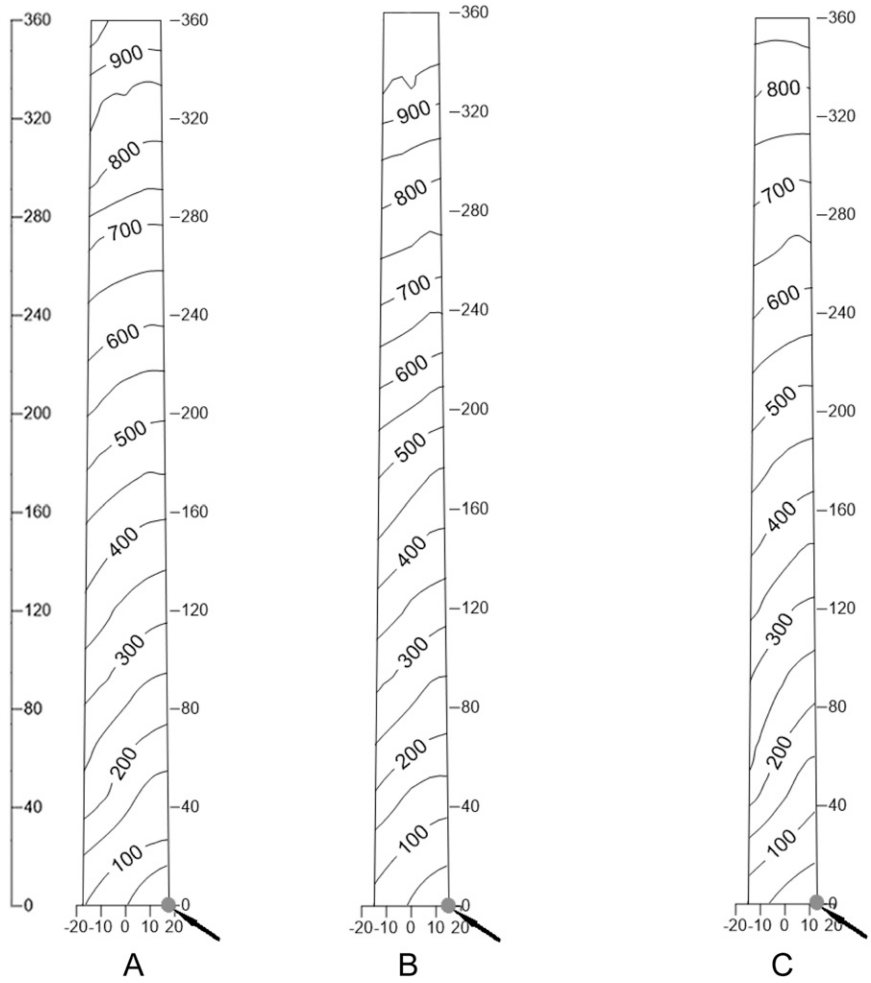

Figure 8. Two-dimensional wave front progression maps obtained from field time-of-flight measurements on log samples (unit: μs; the dot in the lower right corner indicates the wave initiation point).

procedures were repeated on each new cross section. On each log sample, TOF data were obtained on 12 consecutive cross sections.

To mimic log measurements, we inserted the start sensor probe into the large end of a log, close to the center and perpendicular to the cross section; the stop sensor probe was still mounted on the cross section of the small end. The start sensor at the log end was struck by a hammer to introduce an impulse load into the log. The same acoustic wave measurement procedures as those for "tree measurement" were used to obtain a series of TOF data at 12 consecutive cross sections on each log.

The data sets collected at each test point included space coordinates, *x*, *y*, and *z*; and the TOF data between start and stop sensors. A complete data matrix obtained from each log was then used to generate contour maps and illustrate the progression of wave fronts in a time sequence.

RESULTS AND DISCUSSION

Effect of Boundary Conditions

Figure 6 shows the simulation results for a tree model under two different boundary conditions: low-reflection condition (Fig 6[a]) and combination of free and low-reflection condition (Fig 6[b]). The

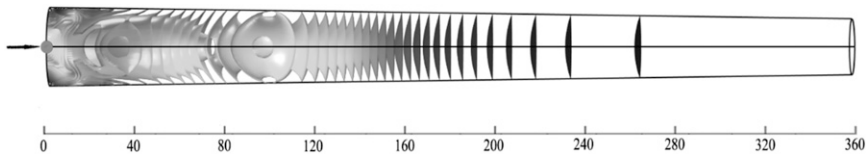

Figure 9. Contour surface map of total displacement in the log model (t = 700 μs).

outputs of post data processing through COMSOL Multiphysics software are contour surface maps of displacements in the tree model at a time sequence t = 100, 200, 300, 400, 500, 600, 700, 800, and 900 μs. The dot in the bottom right corner indicates the impact source. The forefront surface in the displacement contour map is the leading edge of the compression waves, namely, the wave front that defines the boundary between the disturbance zone and undisturbed zone.

Figure 6(a) illustrates the propagation of acoustic waves in the tree model under a low-reflection boundary condition, where the waves were not reflected when they encountered the side boundaries. The impulse wave initially expanded mostly in radial and tangential directions and then gradually shifted toward the longitudinal direction. The wave front under the low-reflection boundary condition appeared to maintain a spherical shape during the course of propagation. This simulation result is very different from what was reported in previous studies (Su et al 2009; Zhang et al 2009; Searles 2012), where the experimental results showed that the wave front became flattened as the waves traveled through a certain distance. It has also been reported that in steel, when a bullet was fired against the lower end of the cross section, the stress from the impulse load became evenly distributed over the cross section at 4-5 diameters from the impact point (Karman 1958). Through TOF measurements of three red pine logs, Zhang et al (2011) found that stress became evenly distributed after approximately 10 diameters from the impact point.

By contrast, Fig 6(b) illustrates the propagation of compression waves in the tree model under free (side) and low-reflection (ends) boundary conditions. In this case, the resulting contour map is a complex mixture of the compression waves moving along the tree model and the waves reflected from the sides (free boundary). It is noted that the shape of the wave front clearly became flattened and turned toward the horizontal direction (but not exactly) when the compression waves moved up in the tree model. This indicates that the longitudinal compression waves become the dominating waves that continuously propagate upward in the tree model, which is consistent with experimental results from three freshly cut red pine logs reported by Su et al (2009) and Zhang et al (2009) and the results from three freshly cut Sitka spruce logs reported by Searles (2012).

Given the fact that a standing tree trunk is free from any constraints or load on the side surface, and the model domain is limited to a certain length (3.6 m in this study), the free boundary for the side surface and low reflection for the two ends were deemed appropriate and thus adopted for all simulations thereafter.

Wave Propagation Patterns in Tree Models

Numerical simulation. To visually illustrate the propagation patterns of acoustic waves in the tree model, we developed a progression map of wave fronts by extracting the forefront contour surface from the displacement contour maps at various time points: 100, 200, 300, 400, 500, 600, 700, 800, and 900 μs. The map is essentially a cluster of leading contour surfaces where the arrival time is the same at any point of the surface (isochronous surface). Therefore, it illustrates the wave fronts in a tree model in a time sequence (Fig 7).

The wave front progression map shows that the acoustic waves initially traveled in a quarter-ellipsoidal wave front in the impact direction; the

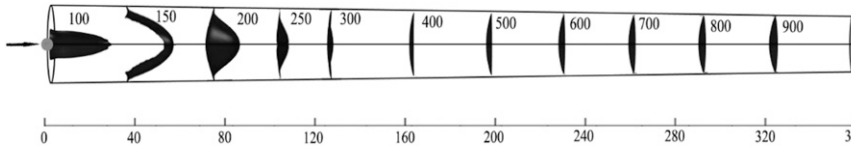

Figure 10. Contour surface maps of displacements in the log model ($t = 100$, 200, 300, 400, 500, 600, 700, 800, and 900 μs).

propagation path then gradually shifted toward the longitudinal direction as the waves moved up in the tree model, guided by the cylindrical shape of the tree model. As the waves propagated further up along the tree model, both the curvature and gradient of the wave fronts gradually decreased and the wave fronts approached a quasi-plane close to perpendicular to the tree axis. This wave propagation pattern implies that the acoustic waves initially expanded in a three-dimensional context (case of dilatational waves); then, the waves gradually transformed into a quasi–one-dimensional wave (plane wave). There are no clear criteria to define the transition from dilatational waves to plane waves in such a tree model. However, for the given diameter of the tree model, the dilatational waves appeared to exist within 0- to 1.2-m transit distance; quasi-plane waves were formed well outside 2.4-m transit distance; the nature of wave propagation within the middle section of the tree model, 1.2 to 2.4 m, is complex and cannot be simply explained by Eqs (7) or (11).

Experimental validation. Figure 8 shows two-dimensional progression maps of the wave fronts obtained from the field TOF measurements conducted on three log samples of different diameters (38, 32, and 28 cm large end). The values shown on the TOF contour lines (wave fronts) are in microseconds. The dot in the lower right corner indicates the impact initiation point. The experimental results revealed wave propagation patterns similar to the numerical simulations. The wave fronts exhibit large curvatures and gradients in the early stage of wave propagation (0- to 1.2-m transit length). The curvature of the wave fronts then gradually decreased, and the wave front became flattened as it moved further away from the impact source, but the gradient of the wave fronts maintained somewhat constant. As the waves moved close to a 3.6-m transit distance (the length of log samples), the wave fronts became close to perpendicular to the longitudinal axis.

Comparing with the simulation results in Fig 7, the measured TOF contours in Fig 8 show significant irregularities, which were primarily caused by the anisotropy and inhomogeneity of wood properties due to natural growth defects. Acoustic waves are highly sensitive to grain orientation and local defects such as knots and grain distortion. The waves advance in the direction of grain and drag as they encounter knots (Gerhards 1982). The numerical simulations in this study, on the other hand, were based on ideal tree models of the orthotropic material and thus resulted in relatively uniform patterns. In general, the wave front mappings obtained from TOF measurements on log samples were found consistent with the simulation results, indicating that the numerical simulation of wave propagation in tree models using COMSOL software is a valid approach and the simulation results are accurate and reliable.

Wave Propagation Patterns in Log Models

Numerical simulation. Figure 9 shows simulation results for a log model under low-reflection (ends) and free boundary (sides) conditions. Similar to the tree modeling, the outputs of simulations are contour surface maps of displacements in the log model as the wave propagation time reached 700 μs. The forefront surface in the displacement contour map is the leading edge of the compression waves. The resulting contour map shows that the wave front in the log model

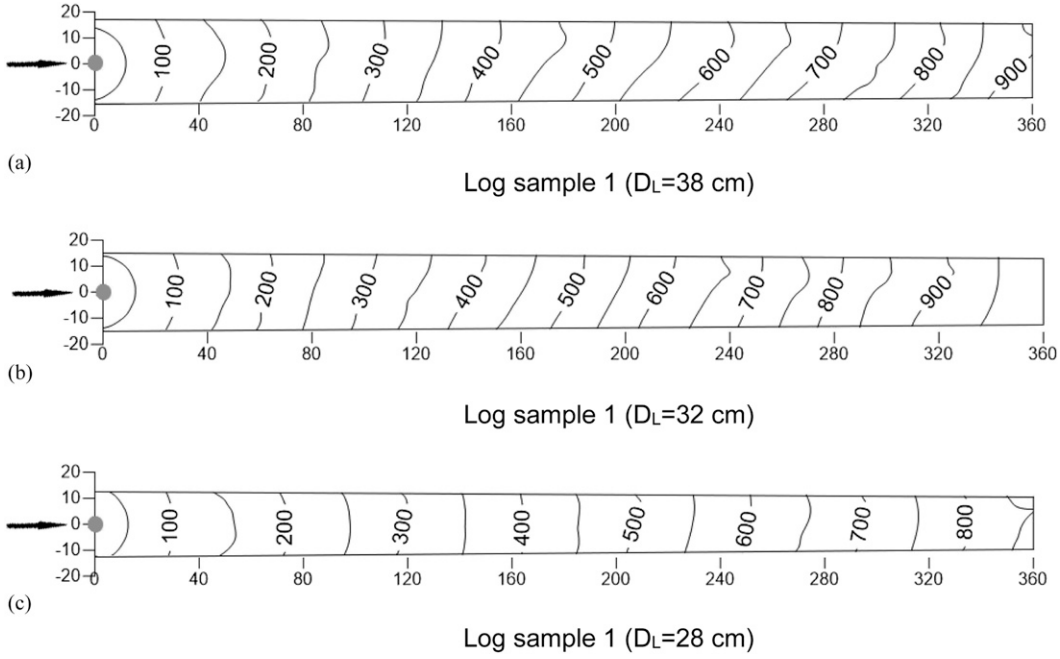

Figure 11. Two-dimensional wave front progression maps of log samples developed through time-of-flight measurements.

maintained vertical with respect to the longitudinal axis. The longitudinal compression waves dominated the entire propagation distance with some side reflections in the beginning (transit length of about 1 diameter).

Figure 10 shows the wave front progression map for the log model at various time points: 100, 200, 300, 400, 500, 600, 700, 800, and 900 μs. The wave was initiated at the center of the log end and started as a dilatational wave, with its wave front changing from ellipsoidal at 100 μs to spherical form at 200 μs (about 2 diameters). The wave then quickly transformed into a one-dimensional plane wave, evidenced by the near-plane wave fronts from 300 μs forward (transit distance 1.2 m and beyond). It was also found that the waves traveled faster in the form of dilatational waves, evidenced by the longer transit distance for the same time internal (100 μs) at the early phase and the shorter distances after the wave front became flattened (plane wave).

Experimental validation. Figure 11 shows the two-dimensional wave front progression maps of three log samples ($D_L = 38$, 32, 28 cm) obtained from the field TOF measurements. Similar to the simulation results, the impact wave propagated from the initiation point as a dilatational wave in the beginning, except its wave front started with a spherical form instead of an ellipsoidal form, as observed in numerical simulation. The curvature of the wave fronts then quickly decreased and became somewhat flattened as the waves moved further away from the wave initiation point, which is an indication of the waves becoming quasi-plane waves. Unlike the vertical and near-plane wave fronts observed in numerical simulations, the wave fronts measured in the log samples were not uniform and exhibited some variation. This variation in wave fronts was likely caused by property variations and growth defects such as knots that existed in the log samples. Nevertheless, the wave propagation patterns obtained from the log samples are in a good agreement with the numerical simulations of the log models.

From the experimental results, it is also noted that log diameter seems to have an effect on the shape

Table 2. Tree and log acoustic velocities obtained from both numerical simulations and field time-of-flight measurements.

Method	Model/sample	Diameter (large end) (cm)	Tree velocity (V_T) (m/s)	Log velocity (V_L) (m/s)[a]		Tree-to-log velocity ratio (k)[b]	
				L = 1.2 m	L = 3.6 m	L = 1.2 m	L = 3.6 m
Numerical simulation	Tree model	35	3744	3612	3571	1.037	1.048
Experimental	Log no. 1	38	3734	3549	3487	1.05	1.07
	Log no. 2	32	3688	3478	3411	1.06	1.08
	Log no. 3	28	4010	3883	3754	1.03	1.07
	Average	33	3810.7	3636.7	3550.7	1.048	1.073

[a] L, transit distance (m).
[b] $k = V_T/V_L$.

of wave fronts. The wave fronts in log no. 3, the smallest log ($D_L = 28$ cm), were found to be more flat and uniform than those in logs no. 1 ($D_L = 38$ cm) and no. 2 ($D_L = 32$ cm). This implies that wave propagation velocity in logs could be affected by log diameter for a given transit length. We will further examine the diameter effect on wave propagation velocity through numerical simulation in part 2 of this article series.

Tree Velocity vs Log Velocity

The wave propagation velocity in tree and log models can be calculated based on the transit distance (L_0) and the corresponding fastest arrival time (t_0) derived from the numerical simulations. The fastest arrival time was defined by the leading edge of the wave front, as shown in Fig 6(b).

For the tree model, a transit distance of 1.2 m was used to calculate the wave velocity because this is close to the actual test span used in a typical tree test setup (Wang 1999; Wang et al 2001; Carter et al 2005). For the log model, the wave velocity was calculated for two scenarios: a transit distance of 1.2 m, which corresponds to the tree TOF measurement over the same test span, and a transit distance of 3.6 m, which corresponds to the acoustic resonance measurement over the entire length of the log samples. The second scenario was considered because the log velocity is normally measured in full-length logs using the acoustic resonance method that produces the most accurate velocity measurement in commercial-length logs. As a result, the tree velocity measured over a 1.2-m span has always been evaluated against the velocity measured on the full-length butt logs in various studies (Wang et al 2007b; Carter et al 2005; Wang 2013; Legg and Bradley 2016).

Table 2 summarizes the tree and log acoustic velocities obtained from both numerical simulations and field TOF measurements. The simulation results indicated that the tree velocity was 3.7% higher than the log velocity for 1.2-m transit distance and 4.8% higher than the log velocity for 3.6-m transit distance. These translate into tree-to-log velocity ratios (k_s) of 1.037 and 1.048, respectively. The average "tree velocity" measured on three larch log samples using the TOF method was 3811 m/s, 4.8%, and 7.3% higher than the corresponding measured log velocities for 1.2- and 3.6-m transit distances, respectively. This translates into tree-to-log velocity ratios (k_{TOF}) of 1.048 for the transit distance of 1.2 m and 1.073 for the transit distance of 3.6 m. It is noted that the velocity ratio from numerical simulation (k_s) is slightly lower than that from TOF measurements (k_{TOF}), but they generally agree with each other. The difference could have been caused by the fact that the tree model and actual log samples were not exactly the same in geometry or size; the three log samples had an average diameter (large end) of 33 cm, whereas the tree model was 35 cm in diameter.

Both the tree model simulation and TOF measurements revealed that the wave propagation patterns within the 1.2-m transit distance were mostly dominated by the dilatational waves, evidenced by the wave fronts with large curvatures and expanding both across the tree and along the tree. When the dilatational wave equation for orthotropic materials is applied to the tree model of given material properties (Table 1), the factor k that links

the dilatational wave velocity and one-dimensional plane wave velocity can be theoretically determined based on Eq (9). The theoretical value of k was found to be 1.04 for the tree model, which is very close to the velocity ratios from the numerical simulations. This further supported the hypothesis previously proposed by Wang et al (2007a) and Zhang et al (2011) that the acoustic waves measured in standing trees within the short span (1.2 m) are controlled by dilatational waves or quasi-dilatational waves.

CONCLUSIONS

With the consideration of orthotropic tree model and free and low-reflection boundary conditions, the propagation of acoustic waves in a standing tree can be properly simulated using COMSOL Multiphysics software. The wave front maps of the tree model developed through numerical simulations were found consistent with those obtained through TOF measurements on the log samples, indicating the simulation results are accurate and reliable.

The wave propagation patterns of the tree model revealed that the side-surface–generated acoustic wave expanded as a dilatational wave within 0- to 1.2-m transit distance; as the wave moved up along the tree model, the shape of the wave front gradually flattened and the wave eventually transformed into a quasi-plane wave from 2.4-m transit distance. By contrast, the acoustic wave in the log model expanded as a dilatational wave within a short transit distance (0-80 cm) and then quickly transformed into a plane wave from a 1.2-m transit distance. The tree-to-log velocity ratio from the numerical simulations (k_s) was found to be in a good agreement with both the experimental velocity ratio from field TOF measurements (k_{TOF}) and the theoretical velocity ratio (k) determined by Eq (10), which further supports the hypothesis that the acoustic waves measured in standing trees over a short span (1.2 m) are controlled by dilatational waves or quasi-dilatational waves.

ACKNOWLEDGMENTS

This project was conducted through the research cooperation between Beijing Forestry University and the USDA Forest Service Forest Products Laboratory (11-MU-11111133-031; 18-LI-11111133-024) and was partially funded by the National Natural Science Foundation of China (grant no. 31328005). Financial support to Mr. Fenglu Liu's visiting study in the United States was provided by the China Scholarship Council.

REFERENCES

Addis T, Buchanan AH, Walker JCF (1997) Log segregation into stiffness classes. Pages 7-10 *in* BG Ridoutt, ed. Managing variability in resource quality. FRI Bulletin No. 202, Forest Research Institute, Rotorua, New Zealand.

Addis T, Buchanan AH, Walker JCF (2000) Sorting of logs using acoustics. Wood Sci Technol 34(4):337-344.

Amateis RL (2015) Use of the Fakopp Treesonic acoustic device to estimate wood quality characteristics in loblolly pine trees planted at different densities. *In* Proceedings of the 17th Biennial Southern Silvicultural Research Conference, March 5-7, 2013. e-General Technical Report SRS-203. U.S. Department of Agriculture, Forest Service, Southern Research Station, Asheville, NC. 5 pp.

Amishev D, Murphy GE (2008) Implementing resonance-based acoustic technology on mechanical harvesters/processors for real-time wood stiffness assessment: Opportunities and considerations. Int J For Eng 19(2):48-56.

Andrews M (2003) Which acoustic speed? Pages 156-165 *in* Proceedings of the 13th International Symposium on Nondestructive Testing of Wood, August 19-21, 2002, University of California, Berkeley, CA.

Aratake S, Arima T (1994) Estimation of modulus of rupture (MOR) and modulus of elasticity (MOE) of lumber using higher natural frequency of log in pile of logs II—Possibility of application for Sugi square lumber with pith. Mokuzai Gakkaishi 40(9):1003-1007.

Aratake S, Arima T, Sakoda T, Nakamura Y (1992) Estimation of modulus of rupture (MOR) and modulus of elasticity (MOE) of lumber using higher natural frequency of log in pile of logs—Possibility of application for Sugi scaffolding board. Mokuzai Gakkaishi 38(11):995-1001.

Arima T, Maruymura N, Maruyama S, Hayamura S (1990) Natural frequency of log and lumber hit with hammer and applications for production processing. Pages 527-533 *in* Proceedings of the 1990 International Timber Engineering Conference, October 23-25, 1990, Steering Committee of the 1990 International Timber Engineering Conference, Tokyo, Japan.

Bodig J, Goodman JR (1973) Prediction of elastic parameters for wood. Wood Sci 5(4):249-264.

Bodig J, Jayne BA (1982) Mechanics of wood and wood composites. Van Nostrand Reinhold Company, Inc., New York, NY. 712 pp.

Brashaw BK, Ross RJ, Pellerin RF (1996) Stress-wave nondestructive evaluation of green veneer: Southern yellow pine and Douglas fir. Nondestructive evaluation techniques for aging infrastructure and, manufacturing. Inter Soc Opt Photonics 2944:296-306.

Carter P, Briggs D, Ross RJ, Wang X (2005) Acoustic testing to enhance western forest values and meet customer wood quality needs. General Technical Report PNW-GTR-642, Productivity of western forests: A forest products focus. USDA Forest Service Pacific Northwest Research Station, Portland, OR. pp. 121-129.

Carter P, Chauhan SS, Walker JCF (2006) Sorting logs and lumber for stiffness using director HM200. Wood Fiber Sci 38(1):49-54.

Carter P, Lausberg M (2003) Application of Hitman acoustic technology—The Carter Holt Harvey Experience. FIEA paper. 6 pp.

Chauhan SS, Walker JCF (2006) Variation in acoustic velocity and density with age, and their interrelationships in radiata pine. For Ecol Mgmt 229(1-3):388-394.

Cohen M, Jennings PC (1983) Chapter 7. Silent boundary methods for transient analysis. *In* T Belytschko and TJR Hugues, eds. Computational methods for transient analysis. Computational methods in mechanics, v1. North-Holland, Amsterdam, The Netherlands. 523 pp.

Forest Products Laboratory (2010) Wood Handbook—Wood as an engineering material. General Technical Report FPL-GTR-190. U.S. Department of Agriculture, Forest Service, Forest Products Laboratory, Madison, WI. 508 pp.

Gerhards CC (1982) Effect of knots on stress waves in lumber. Research Paper FPL-384. U.S. Department of Agriculture, Forest Service, Forest Products Laboratory, Madison, WI. 28 pp.

Gil-Moreno D, Dan RE (2015) Comparing usefulness of acoustic measurements on standing trees for segregation by timber stiffness. Pages 378-385 *in* Proceedings of the 19th International Nondestructive Testing and Evaluation of Wood Symposium, September 23-25, 2015, Rio de Janeiro, Brazil. USDA Forest Service, Forest Products Laboratory; General Technical Report. Madison, WI. FPL-GTR-239.

Grabianowski M, Manley B, Walker JCF (2006) Acoustic measurements on standing trees, logs and green lumber. Wood Sci Technol 40(3):205-216.

Halabe UB, Bidigalu GM, GangaRao HVS, Ross RJ (1997) Nondestructive evaluation of green wood using stress wave and transverse vibration techniques. Mater Eval 55(9):1013-1018.

Karman TV 1958. Advances in applied mechanics, Vol. 5. Academic Press, New York, NY. 134 pp.

Lalanne B, Touratier M (2000) Aeroelastic vibrations and stability in cyclic symmetric domains. Int J Rotating Mach 6(6):445-452.

Lasserre JP, Mason E, Watt MS (2004) The influence of initial stocking on corewood stiffness in a clonal experiment on 11-year-old *Pinus radiata* [D. Don]. N Z J For Sci 49:18-23.

Lasserre JP, Mason EG, Watt MS (2005) The effects of genotype and spacing on *Pinus radiata* [D. Don] corewood stiffness in an 11-year old experiment. For Ecol Mgmt 205(1-3):375-383.

Lasserre JP, Mason EG, Watt MS (2007) Assessing corewood acoustic velocity and modulus of elasticity with two impact based instruments in 11-year-old trees from a clonal-spacing experiment of *Pinus radiata* [D. Don]. For Ecol Mgmt 239(1-3):217-221.

Legg M, Bradley S (2016) Measurement of stiffness of standing trees and felled logs using acoustics: A review. J Acoust Soc Am 139(2):588-604.

Lindström H, Harris P, Nakada R (2002) Methods for measuring stiffness of young trees. Holz Roh-Werkst 60: 165-174.

Liu F, Jiang F, Zhang J, Zhang H (2015) Twelve elastic constant values of larch forest. J Northwest For Univ 30(6):227-231.

Madhoushi M, Daneshvar S (2016) Predicting the static modulus of elasticity in eastern cottonwood (*Populus deltoides*) using stress wave non-destructive testing in standing trees. Eur J Wood Wood Prod 74(6):885-892.

Matheson AC, Dickson RL, Spencer DJ, Joe B, Ilic J (2002) Acoustic segregation of *Pinus radiata* logs according to stiffness. Ann For Sci 59:471-477.

Matheson AC, Gapare WJ, Ilic J, Wu H (2008) Inheritance and genetic gain in wood stiffness in radiata pine assessed acoustically in young standing trees. Silvae Genet 57(2):56-64.

Meyers MA (1994) Dynamic behavior of materials. Wiley, New York, NY.

Mora CR, Schimleck LR, Isik F, Mahon JM, Clark A III, Daniels RF (2009) Relationship between acoustic variables and different measures of stiffness in standing *Pinus taeda* trees. Can J Res 39(8):1421-1429.

Nanami N, Nakamura N, Arima T, Okuma M (1992a) Measuring the properties of standing trees with stress waves I. The method of measurement and the propagation path of the waves. Mokuzai Gakkaishi 38(8):739-746.

Nanami N, Nakamura N, Arima T, Okuma M (1992b) Measuring the properties of standing trees with stress waves II. Application of the method to standing trees. Mokuzai Gakkaishi 38(8):747-752.

Nanami N, Nakamura N, Arima T, Okuma M (1993) Measuring the properties of standing trees with stress waves III. Evaluating the properties of standing trees for some forest stands. Mokuzai Gakkaishi 39(8):903-909.

Paradis N, Auty D, Carter P, Achim A (2013) Using a standing-tree acoustic tool to identify forest stands for the production of mechanically-graded lumber. Sensors (Basel) 13(3): 3394-3408.

Raymond CA, Joe B, Anderson DW, Watt DJ (2008) Effect of thinning on relationships between three measures of wood stiffness in *Pinus radiata*: Standing trees vs. logs vs. short clear specimens. Can J For Res 38(11):2870-2879.

Ross RJ, Pellerin RF (1988) NED of wood-based composites with longitudinal stress waves. Forest Prod J 38(5):39-45.

Ross RJ, McDonald KA, Green DW, Schad KC (1997) Relationship between log and lumber modulus of elasticity. Forest Prod J 47(2):89-92.

Sharp DJ (1985) Nondestructive testing techniques for manufacturing LVL and predicting performance. Pages 99-108 *in* Proceedings of the 5th Nondestructive Testing of Wood Symposium, September 9-11, 1985, Washington State University, Pullman, WA.

Searles G (2012) Acoustic segregation and structural timber production. PhD thesis, Edinburgh Napier University, Edinburgh, UK. 218 pp.

Su J, Zhang H, Wang X (2009) Stress wave propagation on standing trees—Part 2. Formation of 3D stress wave contour maps. Pages 59-64 *in* Proceedings of the 16th International Symposium on Nondestructive Testing and Evaluation of Wood, October 12-14, 2009, Beijing Forestry University, Beijing, China.

Trejo JLD (2015) Using acoustic measurements and inventory data to estimate stiffness in standing Douglas-fir trees. MS thesis, Oregon State University, Corvallis, OR. 35 pp.

Wang X (1999) Stress wave based nondestructive evaluation methods for wood quality of standing trees. PhD dissertation, Michigan Technological University, Houghton, MI. 187 pp.

Wang X (2013) Acoustic measurements on trees and logs: A review and analysis. Wood Sci Technol 47(5):965-975.

Wang X, Carter P, Ross RJ, Brashaw BK (2007b) Acoustic assessment of wood quality of raw forest materials—A path to increased profitability. Forest Prod J 57(5):6-14.

Wang X, Ross RJ, Carter P (2007a) Acoustic evaluation of wood quality in standing trees. Part I. Acoustic wave behavior. Wood Fiber Sci 39(1):28-38.

Wang X, Ross RJ, Green DW, Brashaw BK, Englund K, Wolcott M (2004a) Stress wave sorting of red maple logs for structural quality. Wood Sci Technol 37(6):531-537.

Wang X, Ross RJ, Mcclellan M, Barbour RJ, Erickson JR, Forsman JW, McGinnis GD (2001) Nondestructive evaluation of standing trees with a stress wave method. Wood Fiber Sci 33(4):522-533.

Wang XP, Ross RJ, Punches J, Barbour RJ, Forsman JW, Erickson JR (2003) Evaluation of small-diameter timber for value-added manufacturing—A stress wave approach. Pages 91-96 *in* Proceedings of the 2th International Precision Forestry Symposium, June 15-17, 2003, University of Washington College of Forest Resources, Seattle, WA.

Zhang H, Wang X, Ross RJ (2009) Stress wave propagation on standing trees—Part 1. Time-of-flight measurement and 2D stress wave contour maps. Pages 53-58 *in* Proceedings of the 16th International Symposium on Nondestructive Testing and Evaluation of Wood, October 12-14, 2009, Beijing Forestry University, Beijing, China.

Zhang H, Wang X, Su J (2011) Experimental investigation of stress wave propagation in standing trees. Holzforschung 65(5):743-748.